

Infrared Cloud Monitoring with UCIRC2

Rebecca Diesing,^{a,*} Stephan S. Meyer,^a Johannes Eser,^a Alexa Bukowski,^a Alex Miller,^a Jake Apfel,^a Gerard Beck^a and Angela V. Olinto^a for the JEM-EUSO collaboration

^a*Department of Astronomy & Astrophysics, KICP, EFI, The University of Chicago, IL 60637, USA*

E-mail: rrdiesing@uchicago.edu

The second generation of the Extreme Universe Space Observatory on a Super Pressure Balloon (EUSO-SPB2) is a balloon instrument that searched for ultra high energy cosmic rays (UHECRs) with energies above 1 EeV and very high energy neutrinos with energies above 1 PeV. EUSO-SPB2 consists of two telescopes: a fluorescence telescope pointed downward for the detection of UHECRs and a Cherenkov telescope toward the limb for the detection of PeV-scale showers produced by neutrino-sourced tau decay (just below the limb) and by cosmic rays (just above the limb). Clouds inside the fields of view of these telescopes—particularly that of the fluorescence telescope—reduce EUSO-SPB2’s geometric aperture. As such, cloud coverage and cloud-top altitude within the field of view of the fluorescence telescope must be monitored throughout data-taking. The University of Chicago Infrared Camera (UCIRC2) monitored these clouds using two infrared cameras centered at 10 and 12 μm . By capturing images at wavelengths spanning the cloud thermal emission peak, UCIRC2 measured cloud color-temperatures and thus cloud-top altitudes. In this contribution, we provide an overview of UCIRC2, including an update on its construction and performance. We also show first results from the flight.

38th International Cosmic Ray Conference (ICRC2023)
26 July - 3 August, 2023
Nagoya, Japan



*Speaker

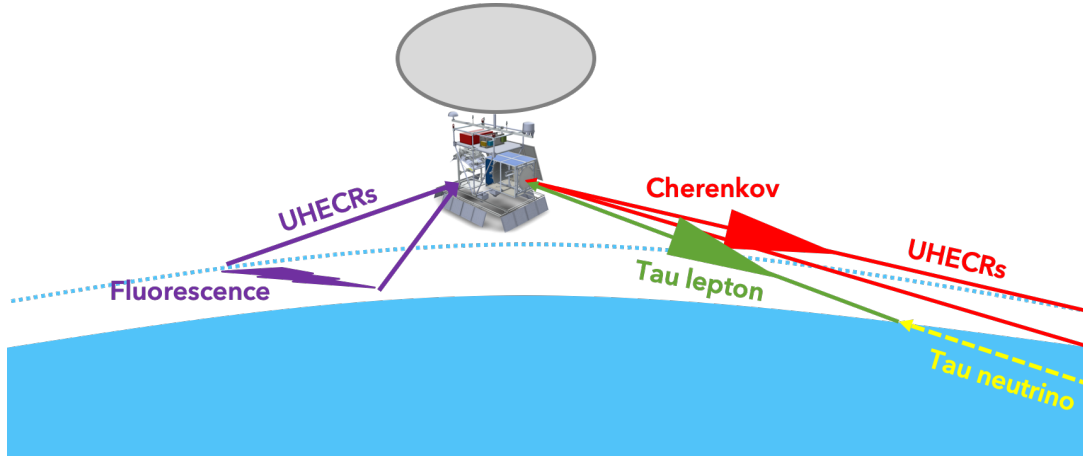


Figure 1: EUSO-SPB2's three detection modes: fluorescence from UHECRs (purple), Cherenkov from UHECRs (red), and Cherenkov from CNs (green).

1. Introduction

Ultra High Energy Cosmic Rays (UHECRs), cosmic rays (CRs) with energies above 10^{18} eV, are currently detected with ground-based observatories such as the Telescope Array [5] in Utah and the Pierre Auger Observatory [4] in Argentina. In particular, UHECRs can be detected via the characteristic particle shower, called an Extensive Air-Shower (EAS), that occurs when an UHECR interacts with Earth's atmosphere. This EAS produces fluorescence of atmospheric nitrogen molecules, detectable in the 300-400 nm spectral band, as well as optical Cherenkov light. Because UHECRs are rare, (< 1 per km^2 per century close to 10^{20} eV), charged-particle astronomy requires extremely large detector volumes. One way to increase detector volume is to observe the atmosphere from above. This technique was tested by the Extreme Universe Space Observatory on a Super Pressure Balloon (EUSO-SPB2) during a brief flight in the spring of 2023.

A pathfinder to a more ambitious satellite mission, EUSO-SPB2 can detect UHECRs via two complementary techniques: looking down upon the atmosphere with a fluorescence telescope and looking towards the limb of the Earth to observe the Cherenkov signals produced by UHECRs above the limb. EUSO-SPB2 also searched for the signatures of neutrinos above 10^{16} eV via the Cherenkov light from upward going tau leptons produced when a tau neutrino interacts near the surface of the Earth (see Figure 1) [1].

The presence of high clouds within the detectors' field of view (FoV)—particularly the fluorescence telescope—can significantly reduce the UHECR event detection rate and event energy calibration. Namely, it is possible for some of the EAS signal to occur behind high clouds. Determining the EUSO-SPB2s exposure to UHECRs thus requires knowledge of the effective detector volume, i.e., the volume of atmosphere within the FoV, above the clouds. Thus, EUSO-SPB2 requires continuous information about cloud coverage and altitude. This is the responsibility of the second generation of the University of Chicago Infrared Camera (UCIRC2). In this proceeding, we present an overview of the UCIRC2 instrument, including preliminary results from its 2023 flight.

2. Method

When EUSO-SPB2 is in observing (night) mode, IR images of the environmental conditions in and around the effective UHECR detection area are captured by UCIRC2 every 120 seconds. These images can be used to collect information about cloud coverage and altitude (cloud top height, CTH) within the field of view of the UHECR detectors (see Figure 2).

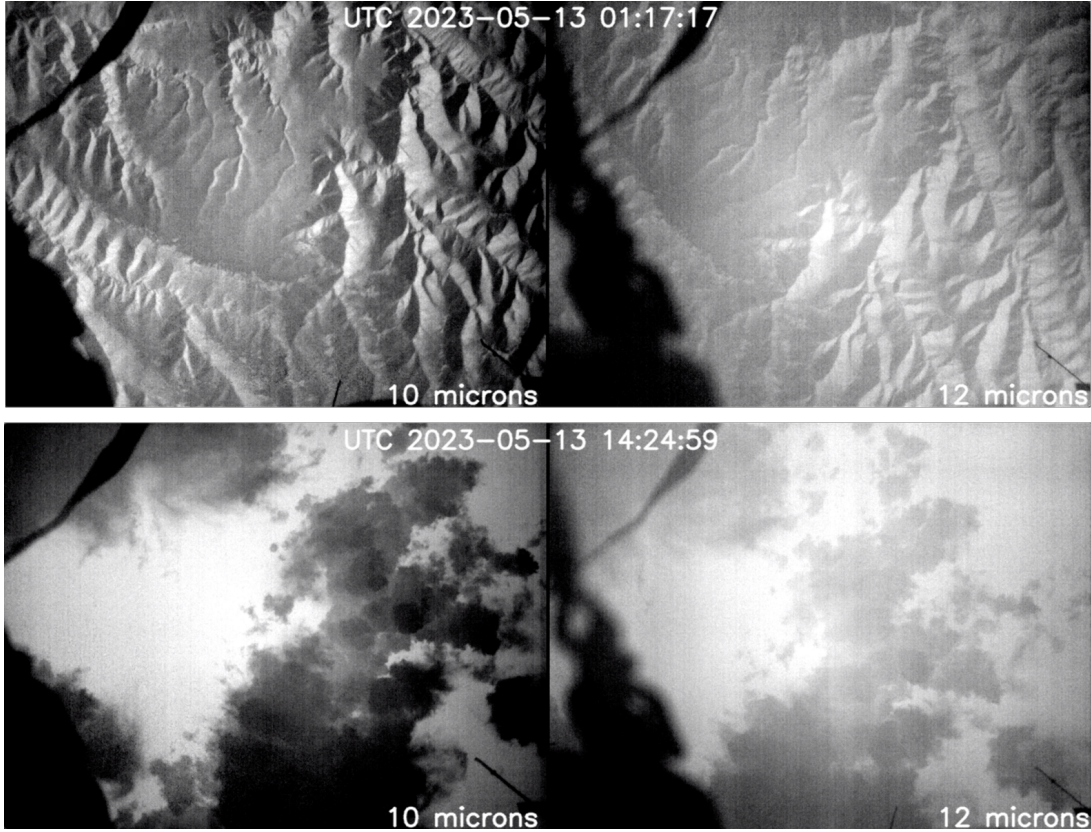


Figure 2: Uncalibrated images of mountains (top) during the daytime and clouds (bottom) during the night captured by UCIRC2, which flew on EUSO-SPB2 in the spring of 2023. Also visible in the foreground is a portion of the EUSO-SPB2 gondola (lower left corners of each image) as well as cables and antennas hanging from the gondola. Using an IR camera, cloud coverage can be easily determined. Cloud temperature (and thus altitude) can be determined by observing at two wavelengths near the cloud blackbody peak, in our case 10 and 12 μm .

Because the clouds are at the temperature of the air, CTH can be inferred from cloud temperature, T_c which can be estimated using two brightness temperatures in bands near in wavelength to the cloud blackbody peak. More specifically, UCIRC2's two IR cameras observe at wavelengths of 10 μm and one at 12 μm . A calibrated image in a single frequency band can be used to determine the temperature of an object of known emissivity (ϵ), but cloud emissivity is highly variable and significantly less than 1. Thus, a multifrequency observation is required to break the degeneracy between ϵ and T_c . For a single layer of clouds above an ocean of known surface temperature and reflectivity (and thus power, P_E), one can estimate power on the detector, P_{tot} as,

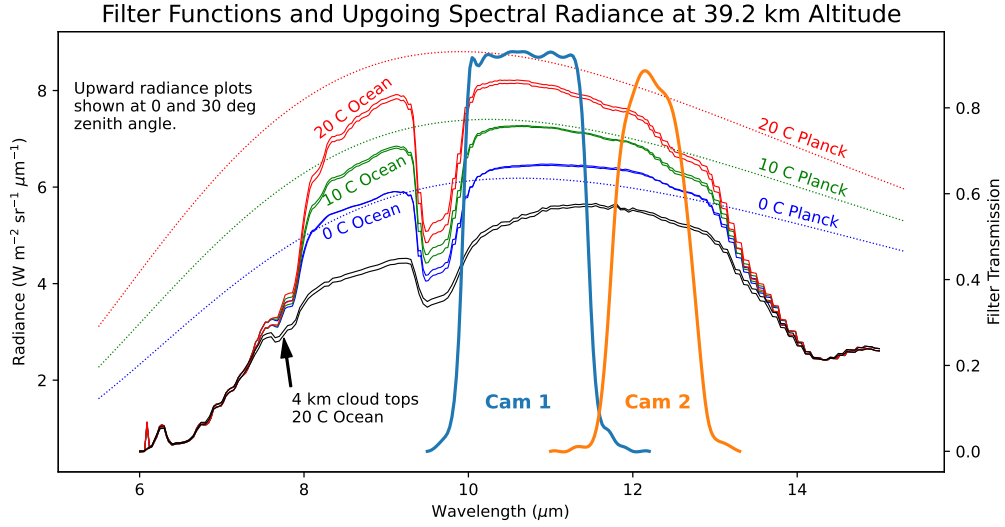


Figure 3: Upgoing spectral radiance as a function of wavelength as calculated using COART [3], assuming different ocean temperatures with no clouds (red, green, and blue lines) and the presence of clouds with tops 4 km above a 20 C ocean (black lines). The two solid lines shown in each case correspond to 0 and 30 degree zenith angles. The blackbody curves corresponding to each ocean temperature are also shown for reference (dotted lines), as are the bandpasses of UCIRC2’s two filters. We will use this model to determine the altitudes of clouds beneath EUSO-SPB2’s fluorescence detector.

$$P_{\text{tot}} = \epsilon P_c + (1 - \epsilon) P_E. \quad (1)$$

Here, P_c is the power of the cloud, from which T_c and thus CTH, can be inferred. Other methods for reconstructing CTH can be found in [2].

For a more precise calculation, we use the Coupled Ocean-Atmosphere Radiative Transfer Model (COART) presented in [3], which calculates the radiance at any frequency by solving the radiative transfer equation from the ocean to a specified level in the atmosphere, including clouds of arbitrary altitude and emissivity (see Figure 3).

3. Design

IR Cameras. UCIRC2 is outfitted with two 640×480 pixel Teledyne DALSA Calibir GXF uncooled IR cameras with 14mm lenses, focused at infinity. The cameras have a $42^\circ \times 32^\circ$ FoV, chosen to be somewhat larger than that of EUSO-SPB2’s fluorescence telescope. When the payload is in “night mode”, which occurs when the atmosphere is dark enough to allow for proper functioning of photodetection modules (PDMs), UCIRC takes a pair of pictures every two minutes. The wide field of view of the IR cameras makes it possible to extrapolate the cloud conditions in the section of the atmosphere swept out by the PDM field of view in the time between pictures.

The native spectral response of the cameras is 8 to 14 μm , but each camera is fitted with a filter to facilitate the radiative CTH reconstruction. One of the cameras is fitted with an Edmund Optics bandpass light filter that transmits wavelengths between 9.6 and 11.6 μm (denoted 10 μm); the other

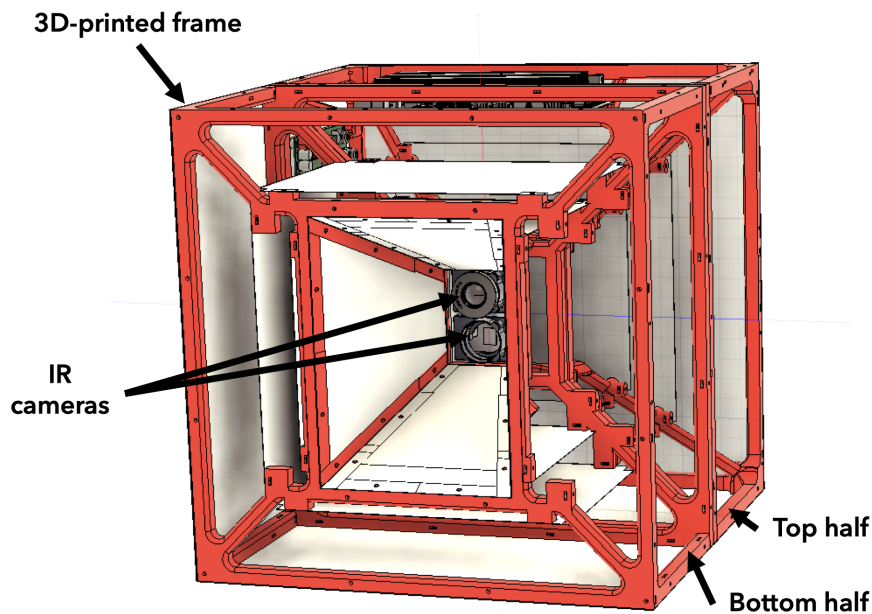


Figure 4: Drawing of UCIRC2, including its 3D-printed frame and two cameras located near the center of the box (pointed toward the viewer). To show the interior structure of the box, this drawing does not include the painted aluminum panels mounted to UCIRC2's sides.

is fitted with a SPECTROGON bandpass light filter which transmits wavelengths between 11.5 and $12.9\mu\text{m}$ (denoted $12\mu\text{m}$). These bands are spaced to obtain brightness temperature data that facilitates both the Blackbody Power Ratio CTH reconstruction and the Radiative Transfer Equation CTH reconstruction methods discussed in the preceding section.

The cameras are powered via a 12V connection and communicate via Gigabit Ethernet with a single-board, industrial-grade CPU that can operate at temperatures between -40C and 85C .

Environment Control. UCIRC2 is designed to operate in a high altitude ($\approx 33\text{km}$) environment during both daytime, when ambient temperatures reaches approximately 40C , and nighttime, when ambient temperatures reach approximately -40C . Temperature management is therefore a central design concern. In particular, the camera response is temperature dependent, meaning that camera temperature must be held approximately constant during operation (night mode). To maintain a stable temperature, the two cameras are housed in a $300\text{mm}\times 300\text{mm}\times 300\text{mm}$ aluminum box coated with high emissivity flat white paint. This box splits into two halves to allow easy access to the cameras and electronics (see Figure 4).

A temperature management system consisting of resistive heaters and thermometers enables precise temperature monitoring and control. This heating system is controlled by a Meerstetter Engineering HV-1123 thermoelectric cooling and heating controller (TEC). Note that system is designed to be most effective at heating because, in general, UCIRC2 collects data during the nighttime, when the environment is cold. The temperature regulated camera stage is a machined

aluminum plate to which both IR cameras are thermally coupled. Note that the set point temperature for the cameras can be modified by telemetry command, with daytime and nighttime operating temperatures chosen to minimize power consumption.

4. Testing and Calibration

To replicate the expected flight environment, UCIRC2 was tested in a thermovac chamber pumped down to 0.3 mbar and a shroud cooled with liquid nitrogen vapor. The temperature management system was tested over all possible environmental temperatures to ensure that the cameras can be maintained within their operating temperature range.

To calibrate the cameras, UCIRC2 was then positioned above a calibration target consisting of a highly emissive, temperature-controlled material. By taking of images of the calibration target at multiple temperatures, this target can be used to perform a pixel by pixel calibration of each camera (see Figure 5). Because the cameras' thermal response depends on their temperature, calibration images were also taken at multiple camera temperatures.

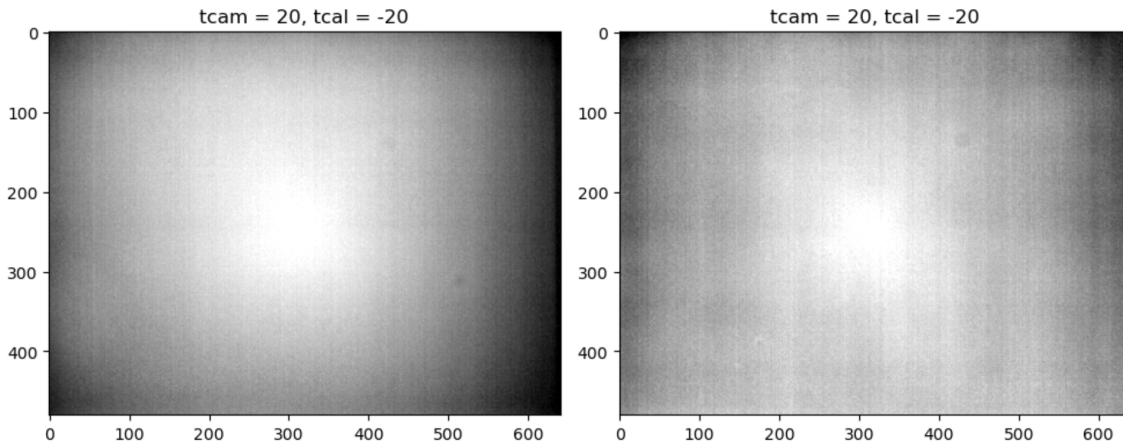


Figure 5: Sample calibration (flat-field) image from each camera, with the camera centered at $10\ \mu\text{m}$ ($12\ \mu\text{m}$) on the left (right), and both the cameras and calibration target set to 20C . The resulting pattern is a camera-specific additive offset, which is subtracted from the images taken during flight.

5. Preliminary Results

Flight Overview. During EUSO-SPB2's brief ($\lesssim 2$ day) flight, UCIRC2 was able to capture one full night's worth of cloud data (i.e., with images captured every two minutes), in conjunction with observations taken by EUSO-SPB2's fluorescence telescope. All of these data were successfully telemetered to the ground. During nighttime operations, UCIRC2 maintained a constant temperature of 10 and later 15C (see Figure 6).

In-Flight Calibration. In addition to the thermovac tests described in the preceding section, we performed in-flight calibration by using the ocean as a flat field. Our method proceeds as follows:

1. Choose a relatively cloud-free image in which the ocean is visible in most pixels.

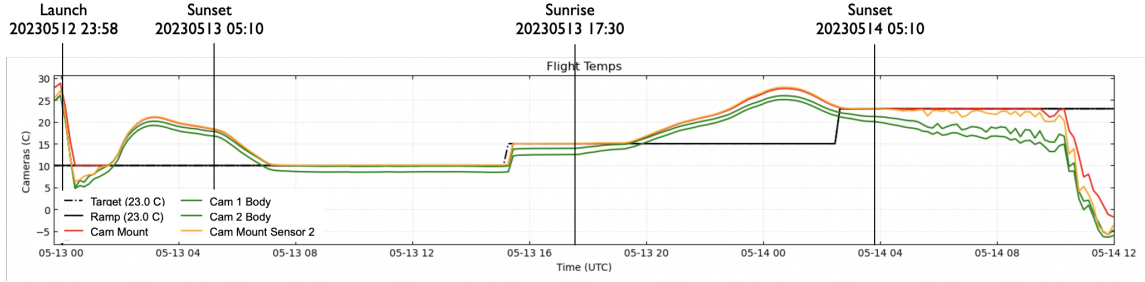


Figure 6: UCIRC2 camera temperatures during flight as a function of time. During nighttime operations, the cameras were maintained at a constant temperature, with control lost only during EUSO-SPB2’s descent.

2. Subtract a flat-field image (I_{ff}) taken in the thermovac (e.g., Figure 5). Use the same calibration data to estimate camera responsivity (counts per unit of radiance) in each pixel (I_r).
3. Using a mask, remove pixels that correspond to foreground objects.
4. Fit the remaining, flat-field subtracted image to a second-order surface, I_{ocean} (i.e., use the ocean as an additional calibrator).

To then calibrate an arbitrary image, I_{init} (i.e., to measure the radiance impinging on in each pixel), we estimate,

$$I_{cal} = \frac{I_{init} - I_{ff} - I_{ocean}}{I_r} + I_{COART}, \quad (2)$$

where I_{COART} is the radiance from a 10 C ocean as a function of zenith angle, as predicted by the COART model described previously. A sample calibrated image is shown in Figure 7.

Outlook. Our calibrated images clearly show cloud coverage, as well as variations in cloud temperature. Going forward, we will use the COART model to make detailed estimates of CTH in order to constrain EUSO-SPB2’s aperture during flight. This exercise will also inform design decisions for IR cameras on future missions to detect EAS’s from above.

6. Acknowledgements

The authors acknowledge the support by NASA awards 11-APRA-0058, 16-APROBES16-0023, 17-APRA17-0066, NNX17AJ82G, NNX13AH54G, 80NSSC18K0246, 80NSSC18K0473, 80NSSC19K0626, 80NSSC18K0464, 80NSSC22K1488, 80NSSC19K0627 and 80NSSC22K0426, the French space agency CNES, National Science Centre in Poland grant n. 2017/27/B/ST9/02162, and by ASI-INFN agreement n. 2021-8-HH.0 and its amendments. This research used resources of the US National Energy Research Scientific Computing Center (NERSC), the DOE Science User Facility operated under Contract No. DE-AC02-05CH11231. We acknowledge the NASA BPO and CSBF staffs for their extensive support. We also acknowledge the invaluable contributions of the administrative and technical staffs at our home institutions.

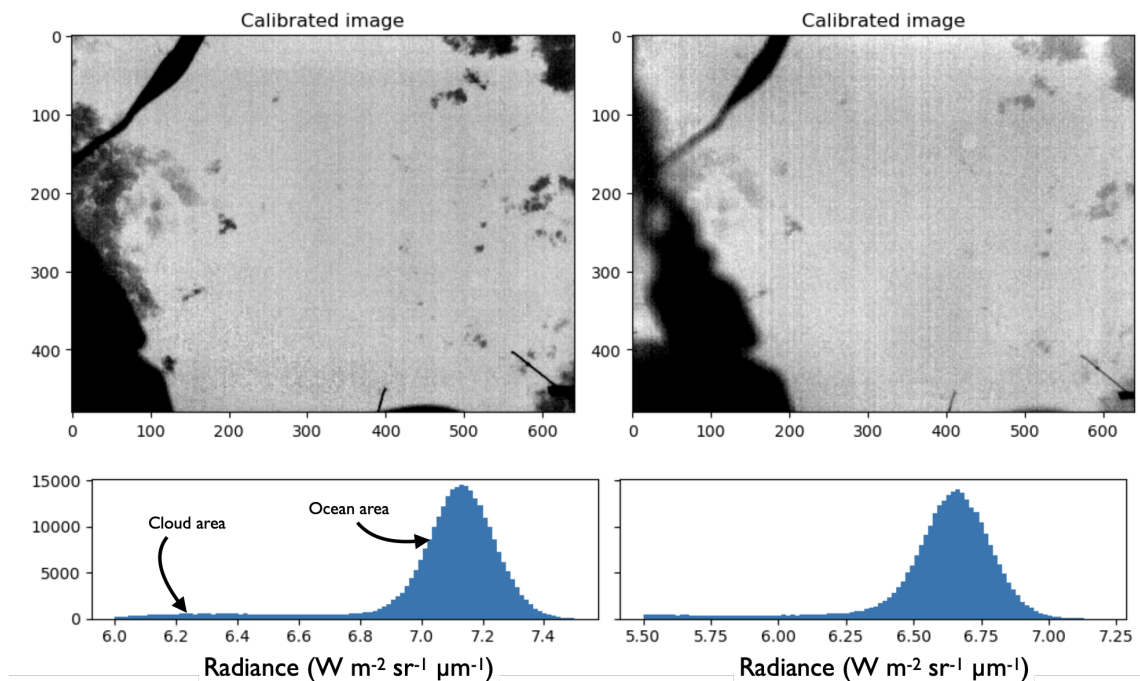


Figure 7: A sample image from each camera (top panels) after applying the calibration technique described in the text. Histograms of the pixels in these images (bottom panels) clearly distinguish between the radiance of the ocean and that of the foreground (clouds, gondola components).

References

- [1] Adams, J. H., Anchordoqui, L. A., Apple, J. A., et al. 2017, White paper on EUSO-SPB2. <https://arxiv.org/abs/1703.04513>
- [2] Anzalone, A., Bertaina, M. E., Briz, S., et al. 2019, IEEE Transactions on Geoscience and Remote Sensing, 57, 304, doi: [10.1109/TGRS.2018.2854296](https://doi.org/10.1109/TGRS.2018.2854296)
- [3] Jin, Z., Charlock, T. P., Rutledge, K., Stamnes, K., & Wang, Y. 2006, Appl. Opt., 45, 7443, doi: [10.1364/AO.45.007443](https://doi.org/10.1364/AO.45.007443)
- [4] Pierre Auger Collaboration. 2015, Nuclear Instruments and Methods in Physics Research Section A: Accelerators, Spectrometers, Detectors and Associated Equipment, 798, 172, doi: <https://doi.org/10.1016/j.nima.2015.06.058>
- [5] Telescope Array Collaboration. 2012, Nuclear Instruments and Methods in Physics Research Section A: Accelerators, Spectrometers, Detectors and Associated Equipment, 689, 87, doi: <https://doi.org/10.1016/j.nima.2012.05.079>

Full Authors list: The JEM-EUSO Collaboration

S. Abe^{ff}, J.H. Adams Jr.^{ld}, D. Allard^{cb}, P. Alldredge^{ld}, R. Aloisio^{ep}, L. Anchordoqui^{le}, A. Anzalone^{ed,eh}, E. Arnone^{ek,el}, M. Bagheri^{lh}, B. Baret^{cb}, D. Barghini^{ek,el,em}, M. Battisti^{cb,ek,el}, R. Bellotti^{ea,eb}, A.A. Belov^{ib}, M. Bertaina^{ek,el}, P.F. Bertone^{lf}, M. Bianciotto^{ek,el}, F. Bisconti^{ei}, C. Blaksley^{fg}, S. Blin-Bondil^{cb}, K. Bolmgren^{ja}, S. Briz^{lb}, J. Burton^{ld}, F. Cafagna^{ea,eb}, G. Cambiè^{ei,ej}, D. Campana^{ef}, F. Capel^{db}, R. Caruso^{ec,ed}, M. Casolino^{ei,ej,fg}, C. Cassardo^{ek,el}, A. Castellina^{ek,em}, K. Černý^{ba}, M.J. Christl^{lf}, R. Colalillo^{ef,eg}, L. Conti^{ei,en}, G. Cotto^{ek,el}, H.J. Crawford^{la}, R. Cremonini^{el}, A. Creusot^{cb}, A. Cummings^{lm}, A. de Castro González^{lb}, C. de la Taille^{ca}, R. DIESING^{lb}, P. Dinaucourt^{ca}, A. Di Nola^{eg}, T. Ebisuzaki^{fg}, J. Eser^{lb}, F. Fenu^{eo}, S. Ferrarese^{ek,el}, G. Filippatos^{lc}, W.W. Finch^{lc}, F. Flaminio^{eg}, C. Fornaro^{ei,en}, D. Fuehne^{lc}, C. Fuglesang^{ja}, M. Fukushima^{fa}, S. Gadamsetty^{lh}, D. Gardiol^{ek,em}, G.K. Garipov^{ib}, E. Gazdálh, A. Golzio^{el}, F. Guarino^{ef,eg}, C. Guépin^{lb}, A. Haungs^{da}, T. Heibges^{lc}, F. Isgrò^{ef,eg}, E.G. Judd^{la}, F. Kajino^{fb}, I. Kaneko^{fg}, S.-W. Kim^{ga}, P.A. Klimov^{ib}, J.F. Krizmanic^{lj}, V. Kungel^{lc}, E. Kuznetsov^{ld}, F. López Martínez^{lb}, D. Mandát^{bb}, M. Manfrin^{ek,el}, A. Marcelli^{ej}, L. Marcelli^{ei}, W. Marszał^{ha}, J.N. Matthews^{lg}, M. Mese^{ef,eg}, S.S. Meyer^{lb}, J. Mimouni^{ab}, H. Miyamoto^{ek,el,ep}, Y. Mizumoto^{fd}, A. Monaco^{ea,eb}, S. Nagataki^{fg}, J.M. Nachtman^{li}, D. Naumov^{ia}, A. Neronov^{cb}, T. Nonaka^{fa}, T. Ogawa^{fg}, S. Ogio^{fa}, H. Ohmori^{fg}, A.V. Olinto^{lb}, Y. Onel^{li}, G. Osteria^{ef}, A.N. Otte^{lh}, A. Pagliaro^{ed,eh}, B. Panico^{ef,eg}, E. Parizot^{cb,cc}, I.H. Park^{gb}, T. Paul^{le}, M. Pech^{bb}, F. Perfetto^{ef}, P. Picozza^{ei,ej}, L.W. Piotrowski^{hb}, Z. Plebaniak^{ei,ej}, J. Posligual^{li}, M. Potts^{lh}, R. Prevede^{ef,eg}, G. Prévôt^{cb}, M. Przybylak^{ha}, E. Reali^{ei,ej}, P. Reardon^{ld}, M.H. Reno^{li}, M. Ricci^{ee}, O.F. Romero Matamala^{lh}, G. Romoli^{ei,ej}, H. Sagawa^{fa}, N. Sakaki^{fg}, O.A. Saprykin^{ic}, F. Sarazin^{lc}, M. Sato^{fe}, P. Schovánek^{bb}, V. Scotti^{ef,eg}, S. Selmane^{cb}, S.A. Sharakin^{ib}, K. Shinozaki^{ha}, S. Stepanoff^{lh}, J.F. Soriano^{le}, J. Szabelski^{ha}, N. Tajima^{fg}, T. Tajima^{fg}, Y. Takahashi^{fe}, M. Takeda^{fa}, Y. Takizawa^{fg}, S.B. Thomas^{lg}, L.G. Tkachev^{ia}, T. Tomida^{fc}, S. Toscano^{ka}, M. Traïche^{aa}, D. Trofimov^{cb,ib}, K. Tsuno^{fg}, P. Vallania^{ek,em}, L. Valore^{ef,eg}, T.M. Venters^{lj}, C. Vigorito^{ek,el}, M. Vrabel^{ha}, S. Wada^{fg}, J. Watts Jr.^{ld}, L. Wiencke^{lc}, D. Winn^{lk}, H. Wistrand^{lc}, I.V. Yashin^{ib}, R. Young^{lf}, M.Yu. Zotov^{ib}.

^{aa} Centre for Development of Advanced Technologies (CDTA), Algiers, Algeria

^{ab} Lab. of Math. and Sub-Atomic Phys. (LPMPs), Univ. Constantine I, Constantine, Algeria

^{ba} Joint Laboratory of Optics, Faculty of Science, Palacký University, Olomouc, Czech Republic

^{bb} Institute of Physics of the Czech Academy of Sciences, Prague, Czech Republic

^{ca} Omega, Ecole Polytechnique, CNRS/IN2P3, Palaiseau, France

^{cb} Université de Paris, CNRS, AstroParticule et Cosmologie, F-75013 Paris, France

^{cc} Institut Universitaire de France (IUF), France

^{da} Karlsruhe Institute of Technology (KIT), Germany

^{db} Max Planck Institute for Physics, Munich, Germany

^{ea} Istituto Nazionale di Fisica Nucleare - Sezione di Bari, Italy

^{eb} Università degli Studi di Bari Aldo Moro, Italy

^{ec} Dipartimento di Fisica e Astronomia "Ettore Majorana", Università di Catania, Italy

^{ed} Istituto Nazionale di Fisica Nucleare - Sezione di Catania, Italy

^{ee} Istituto Nazionale di Fisica Nucleare - Laboratori Nazionali di Frascati, Italy

^{ef} Istituto Nazionale di Fisica Nucleare - Sezione di Napoli, Italy

^{eg} Università di Napoli Federico II - Dipartimento di Fisica "Ettore Pancini", Italy

- eh* INAF - Istituto di Astrofisica Spaziale e Fisica Cosmica di Palermo, Italy
ei Istituto Nazionale di Fisica Nucleare - Sezione di Roma Tor Vergata, Italy
ej Università di Roma Tor Vergata - Dipartimento di Fisica, Roma, Italy
ek Istituto Nazionale di Fisica Nucleare - Sezione di Torino, Italy
el Dipartimento di Fisica, Università di Torino, Italy
em Osservatorio Astrofisico di Torino, Istituto Nazionale di Astrofisica, Italy
en Uninettuno University, Rome, Italy
eo Agenzia Spaziale Italiana, Via del Politecnico, 00133, Roma, Italy
ep Gran Sasso Science Institute, L'Aquila, Italy
fa Institute for Cosmic Ray Research, University of Tokyo, Kashiwa, Japan
fb Konan University, Kobe, Japan
fc Shinshu University, Nagano, Japan
fd National Astronomical Observatory, Mitaka, Japan
fe Hokkaido University, Sapporo, Japan
ff Nihon University Chiyoda, Tokyo, Japan
fg RIKEN, Wako, Japan
ga Korea Astronomy and Space Science Institute
gb Sungkyunkwan University, Seoul, Republic of Korea
ha National Centre for Nuclear Research, Otwock, Poland
hb Faculty of Physics, University of Warsaw, Poland
ia Joint Institute for Nuclear Research, Dubna, Russia
ib Skobeltsyn Institute of Nuclear Physics, Lomonosov Moscow State University, Russia
ic Space Regatta Consortium, Korolev, Russia
ja KTH Royal Institute of Technology, Stockholm, Sweden
ka ISDC Data Centre for Astrophysics, Versoix, Switzerland
la Space Science Laboratory, University of California, Berkeley, CA, USA
lb University of Chicago, IL, USA
lc Colorado School of Mines, Golden, CO, USA
ld University of Alabama in Huntsville, Huntsville, AL, USA
le Lehman College, City University of New York (CUNY), NY, USA
lf NASA Marshall Space Flight Center, Huntsville, AL, USA
lg University of Utah, Salt Lake City, UT, USA
lh Georgia Institute of Technology, USA
li University of Iowa, Iowa City, IA, USA
lj NASA Goddard Space Flight Center, Greenbelt, MD, USA
lk Fairfield University, Fairfield, CT, USA
ll Department of Physics and Astronomy, University of California, Irvine, USA
lm Pennsylvania State University, PA, USA